

Injectable tissue integrating networks from recombinant polypeptides with tunable order

Stefan Roberts¹, Tyler S. Harmon^{2,3}, Jeffrey L. Schaal¹, Vincent Miao¹, Kan (Jonathan) Li⁴, Andrew Hunt¹, Yi Wen¹, Terrence G. Oas⁴, Joel H. Collier¹, Rohit V. Pappu^{1,3} and Ashutosh Chilkoti^{1*}

Emergent properties of natural biomaterials result from the collective effects of nanoscale interactions among ordered and disordered domains. Here, using recombinant sequence design, we have created a set of partially ordered polypeptides to study emergent hierarchical structures by precisely encoding nanoscale order-disorder interactions. These materials, which combine the stimuli-responsiveness of disordered elastin-like polypeptides and the structural stability of polyalanine helices, are thermally responsive with tunable thermal hysteresis and the ability to reversibly form porous, viscoelastic networks above threshold temperatures. Through coarse-grain simulations, we show that hysteresis arises from physical crosslinking due to mesoscale phase separation of ordered and disordered domains. On injection of partially ordered polypeptides designed to transition at body temperature, they form stable, porous scaffolds that rapidly integrate into surrounding tissue with minimal inflammation and a high degree of vascularization. Sequence-level modulation of structural order and disorder is an untapped principle for the design of functional protein-based biomaterials.

Many useful properties of soft polymeric materials emerge from the collective interactions among ordered and disordered domains. This phenomenon is also one of the hallmarks of naturally occurring and designed protein-based materials. Silk fibres, for example, owe their extraordinary combination of elasticity and strength to the interactions among periodically repeated β -sheets and unstructured domains encoded by the primary sequence¹. Similarly, tropoelastin—the soluble precursor of elastin—consists of repeats of unstructured hydrophobic regions interspersed by alanine-rich α -helices². Recent insights into intrinsically disordered proteins (IDPs) highlight the importance of synergy among disordered regions and ordered domains as determinants of function and emergent phase behaviour in multivalent proteins^{3,4}.

To answer how the combination of sequence-encoded order and disorder leads to the emergence of novel macroscopic material properties, nanoscale modules have to be synthesized with molecular precision. The recombinant synthesis of peptide polymers makes it possible to design building blocks with precise, genetic control, enabling ordered and disordered components to be mixed and matched at will within a single polypeptide chain⁵. Here, we report the successful design of modular polypeptides wherein we periodically insert an ordered domain into a disordered polypeptide scaffold. This allows us to uncover the impact of single-chain interactions among ordered domains and disordered regions on macroscopic material properties.

Polymer library design

We chose elastin-like polypeptides (ELPs) as our disordered component. These polymers constitute a family of repetitive polypeptides that are based on a consensus (VPGXG) pentapeptide repeat derived from the disordered regions of tropoelastin. ELPs exhibit tunable lower critical solution temperature (LCST) phase behaviour, and they serve as models of elastomeric disorder^{6,7}.

The sequence-encoded intrinsic disorder of ELPs is thought to be responsible for the observed LCST behaviour^{6,8}. ELPs are biocompatible polymers with numerous applications in protein purification, drug delivery and tissue engineering⁹.

Our design criterion for the incorporation of ordered domains into disordered scaffolds required that the folded state be autonomously achievable within monomeric forms of the ordered domains. This criterion ruled out the choice of domains that fold upon oligomerization or fully folded protein domains that could disrupt the desired modularity. We hence settled on a design based on the exon organization of tropoelastin. Polyalanine helices are an important structural element of tropoelastin, where they combine with disordered domains to produce the elasticity and resilience that make elastin an important component of the extracellular matrix^{10,11}. Because polyalanine sequences are also known to have high intrinsic α -helicity in aqueous systems^{12,13}, they also satisfied our requirements for autonomous folding. We hence hypothesized that recombinant polymers composed of minimalized polyalanine domains doped into an ELP scaffold, mimicking the composition and blocky architecture of tropoelastin², would produce biomaterials with unique, tunable properties.

Four polyalanine helices (H1–5) with different charge distributions were incorporated into three ELPs (E1–3) of varying side chain hydrophobicities at either 6.25%, 12.5%, 25% or 50% of the total amino acid number (Fig. 1a). Polyalanine domain compositions were chosen to maximize helicity while controlling hydrophilicity through charge–charge interactions. ELP compositions were chosen to span a range of LCSTs suitable for in vivo injection⁷. The naming convention for our partially ordered polymers (POPs) specifies the ELP (EX), the helix (HY), and the percentage helicity (Z%): EX-HY-Z%. The molecular weights and purities for all polymers are detailed in Supplementary Table 1 and Supplementary Fig. 1, respectively.

¹Department of Biomedical Engineering, Duke University, Durham, NC, USA. ²Department of Physics, Washington University in St. Louis, St. Louis, MO, USA. ³Department of Biomedical Engineering and Center for Biological Systems Engineering, Washington University in St. Louis, St. Louis, MO, USA.

⁴Department of Biochemistry, Duke University, Durham, NC, USA. *e-mail: chilkoti@duke.edu

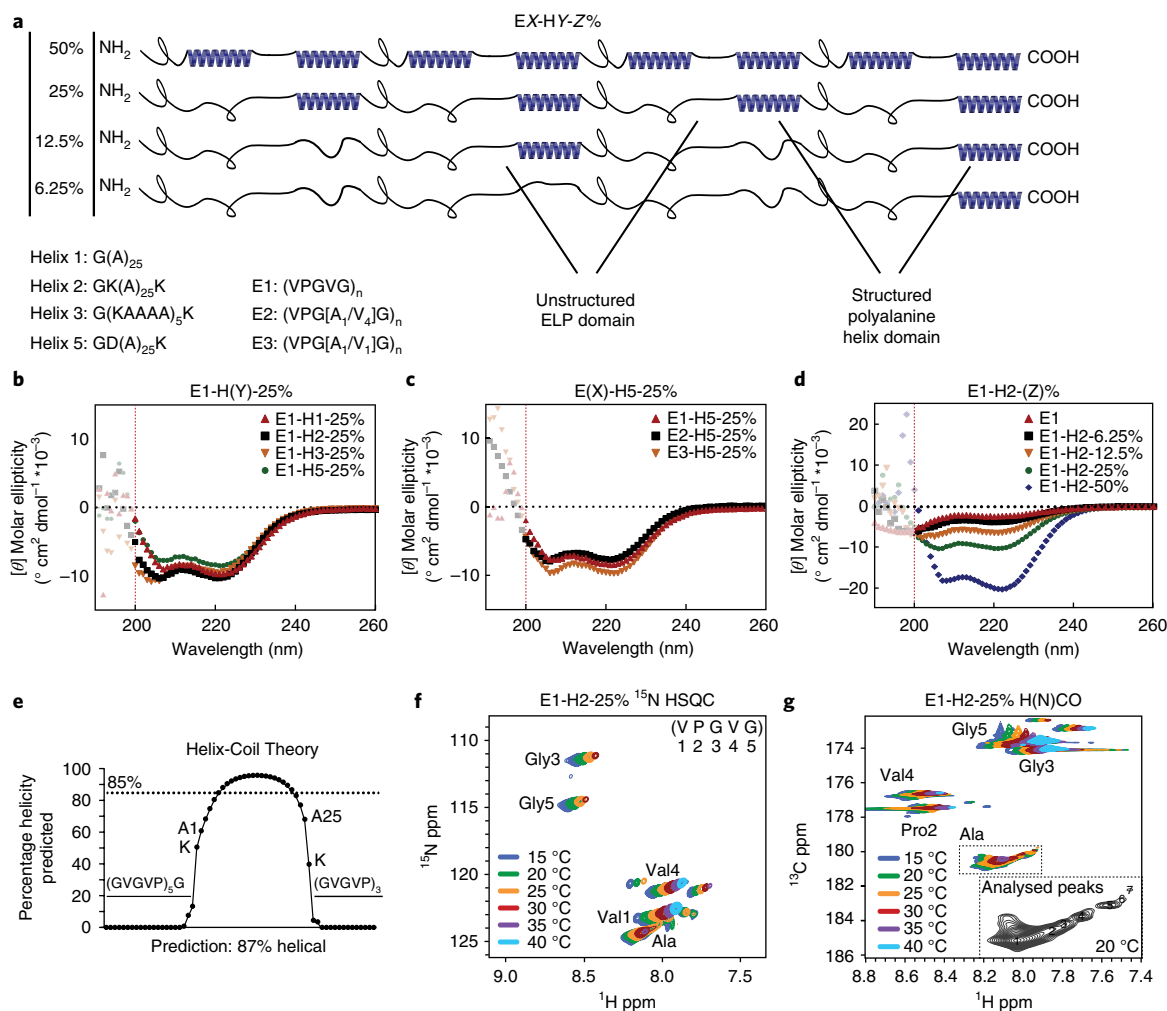


Fig. 1 | Partially ordered polymer library and structural characterization **a**, Recombinant POPs were constructed with three ELP components and four polyalanine helices at amino acid percentages up to 50%. **b–d**, UV-CD reveals definitive helical peaks in molar ellipticity ($[\theta]$) at 222 and 208 nm, with peak amplitudes minimally altered by the type of polyalanine domain (**b**) and ELP (**c**), but highly dependent on total alanine content (**d**) (dynode voltage > 500 V at < 200 nm; data not used for analysis). **e**, This structural signature is consistent with helix-coil predictions (Agadir), as demonstrated for E1-H2. **f,g**, ¹⁵N-HSQC (**f**) and H(N)CO (**g**) (residue labels are the associated C' of the previous residue, axes are chemical shifts in parts per million (ppm)) two-dimensional solution NMR spectra for E1-H2-25% were used to more precisely quantify total structural content. Each polyalanine domain was determined to have an average helicity of 90% (Supplementary Methods).

Structural characterization

We used ultraviolet circular dichroism (UV-CD) to determine POP secondary structure. All POPs show the negative ellipticity peaks at 222 nm and 208 nm (Fig. 1b–d and Supplementary Fig. 2) characteristic of α -helices. Peak magnitudes are largely independent of polyalanine and ELP composition, but are highly dependent on total polyalanine percentage. The helices are thermally stable, with the lowest melting temperatures greater than 65 °C (Supplementary Fig. 2). However, because quantitative analysis of UV-CD (Supplementary Table 2) for disordered proteins is known to be inaccurate^{14,15} and polyalanines can sometimes form β -rich fibrils¹⁶ we also used two-dimensional solution NMR to confirm and quantify POP helicity. Combinations of triple-resonance NMR spectra were used for residue assignment, and helicity was determined on the basis of the backbone carbonyl carbon chemical shifts of identified alanine peaks in the H(N)CO spectra (Fig. 1fg and Supplementary Fig. 3). Analysis of NMR data showed that 90% of the residues within each polyalanine domain are in a helical conformation at 20 °C—a result that is supported by predictions from helix-coil theory (Fig. 1e)^{17,18}.

Sharp phase behaviour and tunable hysteresis

ELPs exhibit reversible LCST behaviour, cycling between an optically clear solution phase and a turbid phase. We measured the thermal phase transition of our POPs by monitoring their optical turbidity as a function of temperature. Remarkably, all proteins demonstrate a very sharp phase transition (1–2 °C) range, even when composed of 50% α -helix (Fig. 2 and Supplementary Fig. 4). These transition temperatures (T_i) vary depending on the specific ELP and helix composition due to differences in their hydrophilicity and charge, but all POPs exhibit the sharp phase behaviour characteristic of fully disordered ELPs.

When turbid POP solutions are cooled, they form clear solutions; however, one aspect of their behaviour was of particular interest—the marked downshift in the inferred T_i during cooling, designated here as T_i -cooling, when compared to the T_i along the heating leg, designated here as T_i -heating. This thermal hysteresis, defined as the difference between T_i -heating and T_i -cooling, or ΔT_i , is not observed in ELPs although it has been advantageous in other recombinant polymers for the development of hyper-stable micro-particles and for stabilizing protein scaffolds^{19–21}. However,

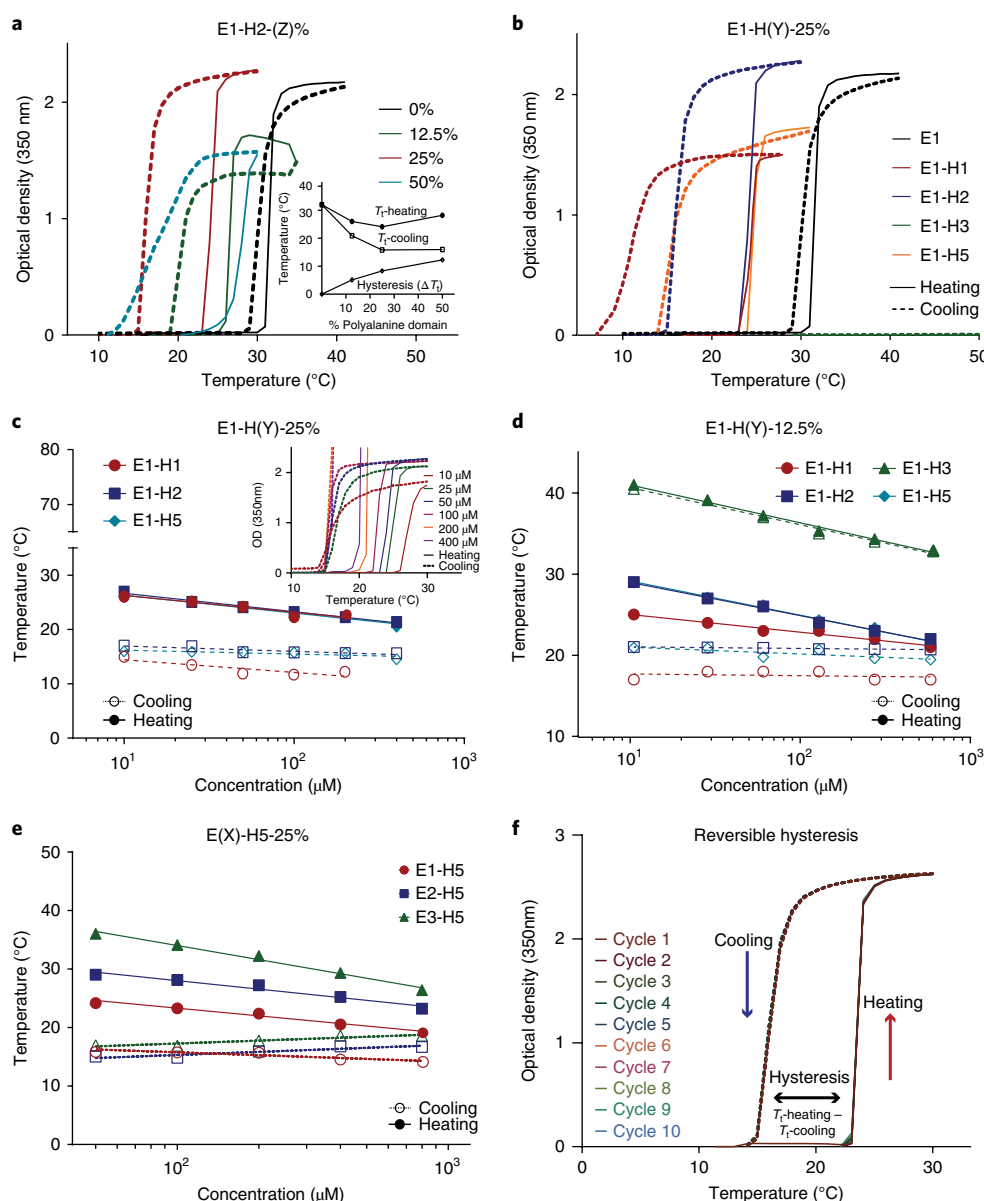


Fig. 2 | Phase behaviour and tunable hysteresis **a**, Optical density (OD) measurements as a function of temperature show sharp, reversible phase behaviour and hysteresis (ΔT_c). Inset: hysteresis scales as a function of total helical content. **b–d**, For a given E(X), hysteresis is also dependent on the composition (charge distribution) of the polyalanine domains, with an increase in charge producing a decrease in hysteresis. The T_c -cooling is independent of concentration (example raw OD measurements for E1-H2-25% given in Fig. 1c inset), and solely determined by the polyalanine domains. **e**, Therefore, for a given H(Y), the T_c -heating can be independently controlled with ELP composition, providing a method to orthogonally control T_c -heating and T_c -cooling. **f**, Polymers can be cyclically heated and cooled with no change in thermal behaviour. Optical density measurements were taken at 350 nm in PBS at 50 μM unless otherwise indicated. Heating and cooling rates were kept at 1 °C min⁻¹. OD amplitudes are non-interpretable due to differences in aggregate formation and settling.

the inability to tune the temperature range over which hysteresis occurs in these systems has severely impeded their application.

In contrast, the thermal hysteresis in POPs can be precisely controlled as it is directly correlated with polymer helicity (Fig. 2a) and is inversely correlated with the amount of charge on the helix side chains (Fig. 2b–d and Supplementary Fig. 4). Importantly, once fully solvated, POPs return to their original state and can be cyclically heated and cooled with no permanent alterations in their solubility (Fig. 2f). By incorporating helices that engender sufficient charge repulsion amongst helices, such as H3, hysteresis can be eliminated altogether. Hysteresis is independent of both heating and cooling

rates, and polymers heated and then cooled to their hysteretic range remain aggregated after 24 h (Supplementary Fig. 5). Subsequent cooling below the T_c -cooling after 24 h causes rapid dissolution.

For POPs, the T_c -heating scales logarithmically with polymer concentration, in accordance with ELP behaviour⁷. However, T_c -cooling is independent of concentration (Fig. 2c–e). Altering the ELP composition adjusts the T_c -heating, but it does not change the T_c -cooling (Fig. 2e). These observations indicate that the composition and chain length of the ELP segment control T_c -heating, whereas the helix composition is the primary determinant for T_c -cooling. Tuning these two independent parameters—composition

of the ELP segment and the fraction and composition (alanine versus charge content) of helix-spanning residues in the POP—provides a sequence-encoded dial to tune the temperature for the onset and range of thermal hysteresis.

These attributes are potentially useful for applications that require hysteresis to encode memory effects. As proof-of-concept for the functional utility of thermal hysteresis, we designed diblock copolymers with a hydrophobic POP and a hydrophilic ELP segment, creating self-assembling nanoparticles with ‘shape-memory’ (Supplementary Fig. 6). The POP–ELP diblock self-assembles upon heating above the T_i -heating of the POP core block, but does not disassemble until below its T_i -cooling. These nanoparticles are hence stable within a hysteretic range, once formed. The rational design of protein nanoparticles with controllable kinetic stability, defined in terms of the value of ΔT_i , may offer an intermediate option for drug delivery between physically crosslinked micelles that disassemble in blood upon dilution below their critical micelle concentration, and chemically crosslinked micelles, which must rely on bond cleavage or protease degradation for drug release.

A molecular model for the mechanism of hysteresis

Thermal hysteresis is commonly attributed to changes in secondary structure^{21,22}. Because polyalanine can adopt random coil, polyproline II, α -helical and β -sheet structures²³, we first analysed POPs to determine if hysteresis derives from changes in secondary structure upon aggregation. UV-CD spectra of a hydrophilic POP (E1-H3-25%) indicate that, in the absence of self-associations, the polymers retain a high degree of helicity up to at least 65 °C (Supplementary Fig. 2). Phase separating POPs show distortions in the UV-CD spectra consistent (Supplementary Fig. 7) with those observed for helical bundles of tropoelastin^{24,25}. These spectral shifts suggest the presence of bundled helices within the POP assemblies. This observation is consistent with the coacervation of tropoelastin, in which polyalanine domains retain their structural integrity during coacervation to stabilize side-chain interactions for crosslinking^{26,27}.

Given the intrinsic tendency of polyalanine to form helical bundles^{12,16} and the persistence of helices within POP aggregates, we propose helical bundling as a significant contributor to hysteresis. To test this proposal, we performed proof-of-concept assessments using coarse grain molecular dynamics simulations. We used a phenomenological model separating the protein domains into two categories of pentapeptide ‘beads’: polyalanine (AAAAA) and ELP (VPGVG). Because polyalanine is observed to self-associate, the interaction energies between polyalanine beads (E_{AA}) are chosen to be favourable and independent of temperature; ELP interaction energies (E_{EE}) change with temperature, increasing in strength above the T_i -heating. ELP–polyalanine interactions (E_{EA}) are always unfavourable.

We simulated a hysteretic cycle for 50 polymers of 25% helicity (E1-H1-25%) in a 25-nm-radius spherical box (Supplementary Information). The results (Fig. 3) suggest that POPs move through four stages during a thermal cycle. In stage 1, below their T_i -heating, POPs are isolated oligomers with local helical clusters solvated by ELPs. In stage 2, above the T_i -heating, localized clusters dock due to the increased favourability of ELP hydrophobic interactions. In stage 3, given sufficient time, alanine domains exchange with neighbouring clusters such that single POPs span multiple clusters, entangling them into a network. Swapping helices between clusters is feasible given their high density in the docked state and is thermodynamically favoured by entropy of mixing. As the temperature increases further and the ELP repulsive term decreases further, a second reversible transition becomes favoured where docked spherical clusters convert into denser, less dynamic linear aggregates—a transition similar to a sphere-to-rod transition for micelles. Above T_i -heating, the ELP domains become less soluble, requiring less surface area. Changes in the ratio of surface area to volume can lead

to a thermodynamic preference for rods over spheres²⁸. In stage 4, once cooled below the T_i -heating, the entanglement of aggregates prevents the dissolution of ELP domains, producing entangled oligomers. Unlike the fast and irreversible transition from docked aggregates to entangled aggregates (stages 2 to 3), transitions between entangled oligomers and isolated oligomers are slow. A sufficient drop in ELP interaction energy (below T_i -cooling) leads to solvation of the POPs, diluting the clusters and returning them to their original state.

Formation of solid-like fractal networks

The macroscopic properties of POP aggregates also indicate an aggregation mechanism distinct from the liquid coacervation of disordered ELPs. Rather than a turbid suspension, POPs transition into mechanically stable, opaque aggregates. These aggregates undergo syneresis at high temperatures, cracking and shrinking at temperatures considerably above the T_i -heating (Fig. 4a). Syneresis suggests percolated crosslinking interactions among polymers²⁹, probably due to network formation from the helical clustering predicted by our simulations.

We performed oscillatory rheology on POPs to characterize key mechanical network properties and compare them to ELP controls (Supplementary Figs. 8,9). Frequency sweeps in the linear viscoelastic region of ELPs above their T_i show their loss modulus (G'') (23 Pa, 1 Hz, 10 wt%) to be greater than the storage modulus (G') (8.0 Pa, 1 Hz, 10 wt%) and both to be proportional to frequency. This behaviour is consistent with liquid-like coacervates³⁰. In contrast, at equivalent concentrations, POPs exhibit a G' (12.2 kPa, 1 Hz) that is much greater than G'' (0.36 kPa, 1 Hz), close to three orders of magnitude higher than the G' of equivalent ELPs, and independent of frequency. This behaviour is typical of more solid-like materials³⁰. POPs also exhibit high viscosity with plastic, shear-thinning flow, whereas ELPs behave as Newtonian fluids. The shear-thinning slope for POPs is unusually high (−0.95) for long-chain polymers, indicative of some network rupture, and this observation is consistent with reported values for tropoelastin networks³⁰.

Importantly, POP mechanical properties can be altered with polymer composition (Supplementary Fig. 9). Material stiffness is directly correlated with molecular weight and helical percentage but is unaffected by the composition of the disordered region. Although POP aggregate stability is driven by physical crosslinking, other crosslinking mechanisms may also be used to further modulate mechanical properties. The effect of chemical crosslinking on POPs and the relationship to other chemically crosslinked disordered polymers is detailed in the Supplementary Information.

The incorporation of helical domains in POPs also affects microscale phase separation (Fig. 4b,c). Whereas ELPs form micrometre-sized coalescing aggregates, forming a colloidal suspension of liquid-like droplets, POPs undergo arrested phase separation into porous networks. POPs with only a single helix form coacervates similar to fully disordered ELPs (Supplementary Fig. 11), indicating that physical crosslinks between helical domains from separate POP chains are necessary for network formation. These networks have a fractal-like architecture, with E1-H5–12.5% and E1-H5–25% POP networks having fractal dimensions between 1.6 and 1.9, dependent on POP concentration (Supplementary Fig. 10). This fractal dimension is comparable to that observed for native elastin networks³¹. We highlight the fractal nature of POP networks as an intriguing observation because fractals are ubiquitous in nature yet difficult to recreate artificially. Beyond biomimicry, we make no claims for their utility at this time.

We next used structured illumination microscopy (SIM), a super-resolution microscopy technique³², to further characterize POP networks. SIM reveals the presence of interconnected mesoscale polymer globules no larger than 200 nm (Fig. 4d). This architecture is consistent across multiple polymer compositions (Supplementary Fig. 12)

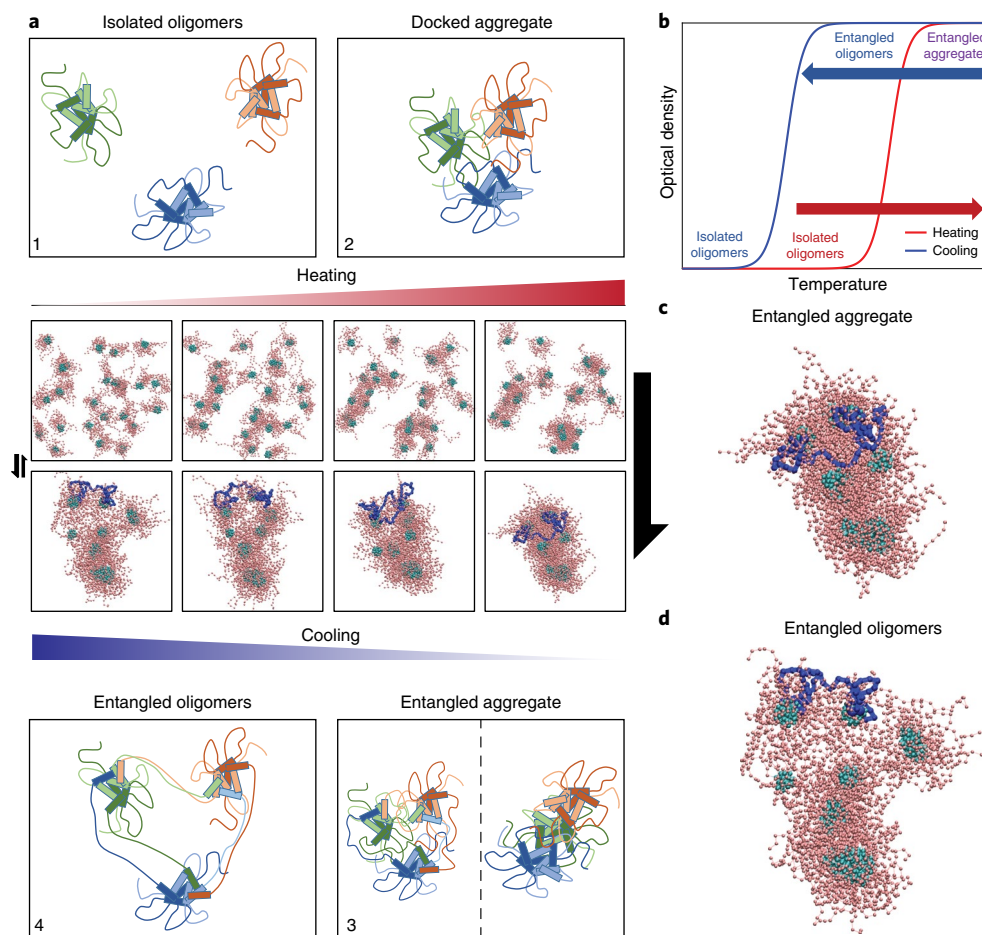


Fig. 3 | Proposed mechanism for hysteresis **a**, Simulations of the hysteretic cycle were performed using a coarse-grained bead-spring model for the POPs. Heating and cooling were achieved by modulating the interaction strengths between ELP domains. The interactions become favourable as temperature increases, and the converse is true on cooling. Snapshots extracted from phenomenological simulations of POPs are shown in the middle, surrounded by cartoon representations of the four states observed for POP during heating and cooling. Rod-like objects represent polyaniline domains and string-like tethers represent ELPs. The colours indicate their initial cluster, with shading indicating different proteins in the same initial cluster. The one-sided arrows provide a pictorial summary of the expected rates for transitions between different states (fast for stage 2 to 3 and slow for stage 4 to 1). Within entangled aggregates we observe two types of morphologies: entangled spheres or entangled cylinders. There is a reversible spheres-to-cylinders transition at even higher temperatures. **b**, Sketch of the experimental observable as a function of heating/cooling—namely, the optical density is annotated by the species populating each regime. **c,d**, Enlarged snapshots from the cooling arm of panel **a** demonstrate that the highlighted POP is not able to isolate itself into a single cluster and that the decrease in aggregate density is limited by the presence of domain swapped proteins.

and suggests a two-stage aggregation process. POPs initially nucleate like their disordered ELP counterparts at their T_i -heating, driven by the disordered domains. Rather than coalesce, as the solution temperature is raised beyond T_i -heating the mesoscopic nuclei rapidly link, forming fractal networks. Our coarse-grained simulations also predict a two-stage process on the nanoscale (aggregate docking and entanglement), and we propose that similar entanglements must also occur on the meso- and micro-scales. This type of aggregation is mirrored in tropoelastin, which undergoes a multistage process²⁷ that includes an initial hydrophobic coacervation into spherical droplets and subsequent maturation into networks or fibres due to interactions between crosslinking domains^{27,33}. Note that the effects of physical crosslinking due to polymer entanglements are notably distinct from those of chemical crosslinking (Supplementary Fig. 13 and Supplementary Discussion).

We also measured the internal mobility of POP networks by monitoring their fluorescence recovery after photobleaching (FRAP). Minimal recovery was observed after 30 min, suggesting that POP networks are kinetically stable (Fig. 5a) due to physical

crosslinking from helical bundling within the network. There is slightly more recovery for 12.5% networks compared to 25%, but the unrecovered fraction remains high (86%). We can also control network porosity by modulating polymer concentration. Using three-dimensional reconstructions from confocal microscopy, we evaluated the effects of concentration and polymer composition on total void volume, defined as the non-protein-rich phase of the network. Within a range of 50 μM (1.6 mg ml^{-1}) to 800 μM (25.6 mg ml^{-1}) for E1-H5-(Z)%, the void volume can be tuned between 90% (~30–50 μm pores) and 60% (~3–5 μm pores), with no noticeable difference in void volume observed between the POPs with 12.5% and 25% helical content over all tested concentrations (Fig. 5b,c and Supplementary Fig. 14). We also measured the void volume for a variety of POP compositions and found that polymer composition—including changes to MW, helical percentage, helix sequence and ELP sequence—have no measurable impact on void volume (Supplementary Fig. 15). This finding allows us to tune porosity of the POP network independently of other network properties. Having porosity as an independently tunable parameter

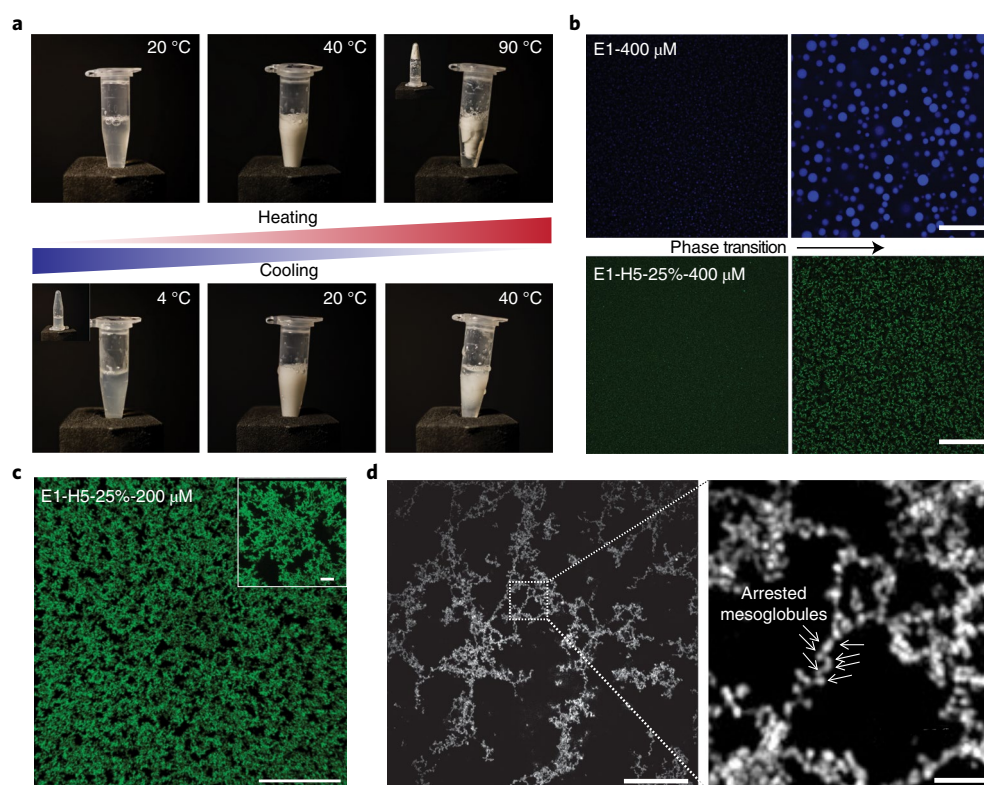


Fig. 4 | Arrested phase separation into fractal networks **a**, E1-H5-25% (2 mM, PBS) aggregation during a heating and cooling cycle shows a reversible transition from an optically translucent liquid to an opaque solid-like structure (passes inversion test) with syneresis observed at higher temperatures. **b**, At the microscale, E1 and E1-H5-25% (400 μM , PBS) form liquid-like coacervates and fractal networks, respectively; scale bar 50 μm . **c**, The intricacy of the network is more clearly seen with a 20- μm -thick three-dimensional reconstruction of E1-H5-25% (200 μM , PBS); scale bars, 50 μm and 10 μm for the inset. **d**, The network architecture at the mesoscale is that of interconnected beads, as revealed by SIM; scale bars 10 μm (left) and 1 μm (right).

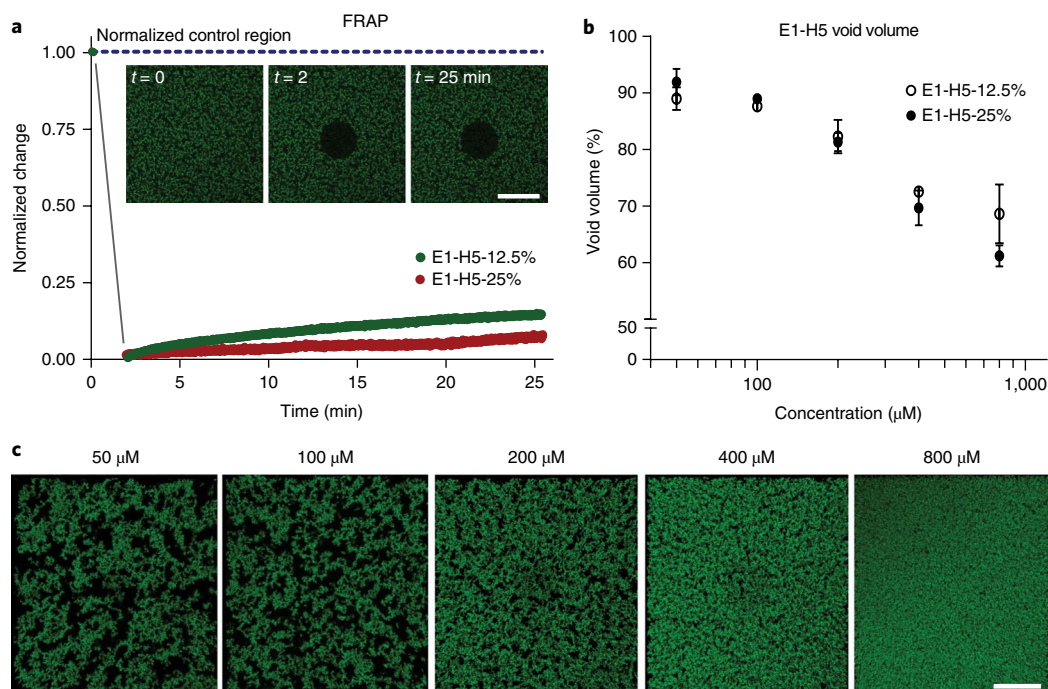


Fig. 5 | Network stability and void volume **a**, As determined by the limited fluorescence recovery 25 min after bleaching, 12.5% and 25% networks have a high kinetic stability and limited liquid-like properties; Inset pictures are shown for E1-H5-25% at 400 μM . **b**, Void volumes can be tuned from 60% to 90% by altering polymer concentration. Data represent mean \pm s.e.m. ($n = 4$ independent samples). **c**, Representative 20- μm -thick image stacks are shown for each measured concentration. Scale bars are 50 μm .

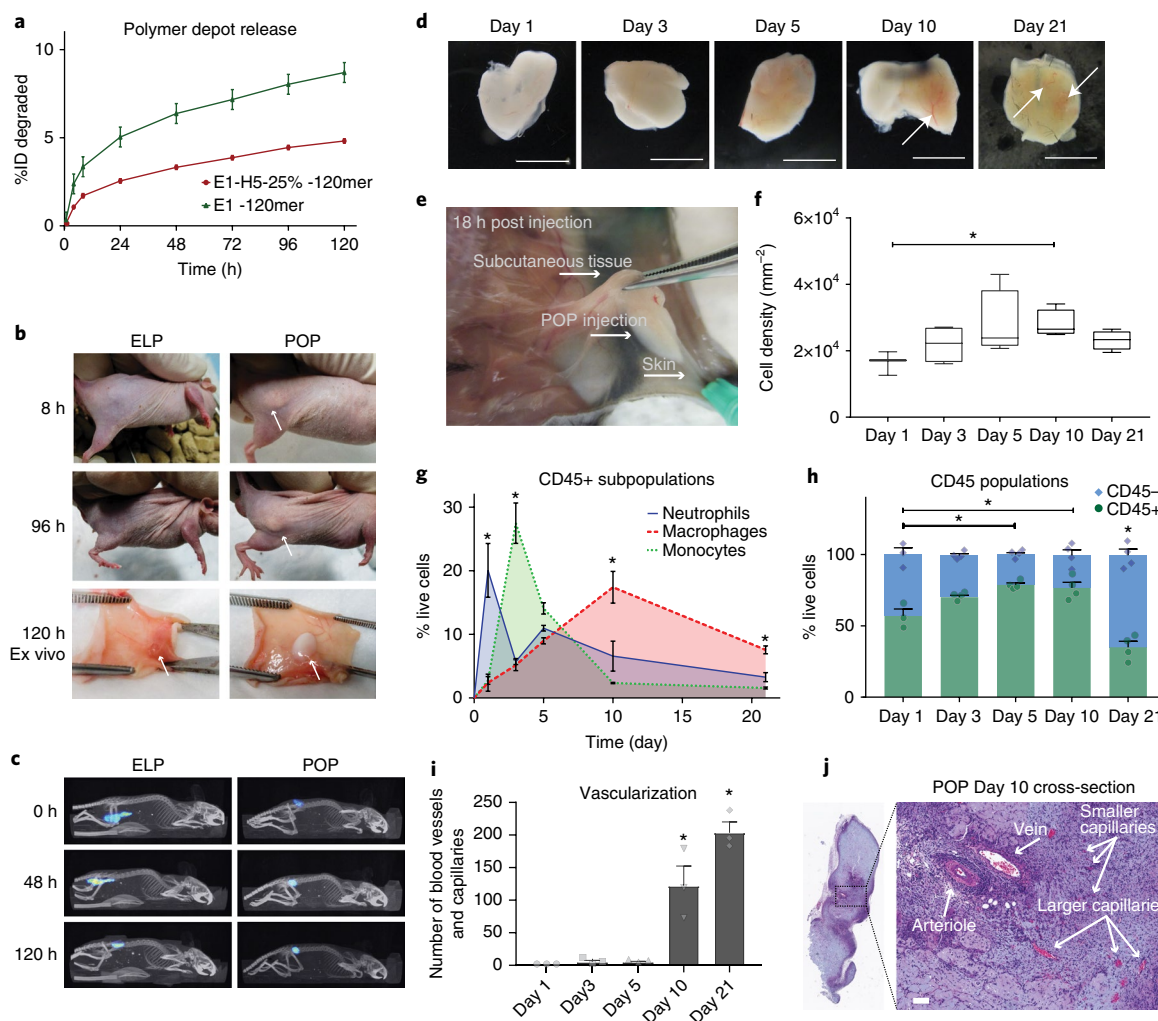


Fig. 6 | In vivo stability and tissue incorporation of POPs **a**, ^{125}I radiolabelled E1-H5-25% POP subcutaneous injections were significantly more stable than their E1 counterparts, with just 5% of the injected dose (ID) degraded at 120 h; 200 μl 250 μM injections; $p < 0.05$ for all data points after 0 h, determined by two-tailed t-tests ($n = 6$ mice); data represent mean \pm s.e.m. **b**, Whereas ELPs diffuse into the subcutaneous space, POP depots were externally apparent, retaining the shape and volume of the initial injection up to dissection and ex vivo analysis. **c**, Representative CT-SPECT images of the depots confirm increased diffusivity of ELPs and increased stability of POPs. **d**, POPs were injected into BL/6 mice and explanted for analysis over 21 days. Representative images are shown with arrows pointing to externally evident vascularization. Scale bars 5 mm. **e**, POPs rapidly integrated into the subcutaneous environment with sufficient strength to endure moderate extension less than 24 h after injection. **f**, There is a high initial cell incorporation with some change over the observed time periods; for *, $p < 0.05$ determined by ANOVA with Tukey post-hoc (day 1 $n = 3$, days 3–21 $n = 4$); data presented as 10–90% box plots. **g**, Flow cytometry for cells involved in innate immunity reveals subsequent spikes in neutrophils, inflammatory monocytes, and macrophages, with a loss in all haematopoietic cells (CD45+) by day 21; for *, $p < 0.05$ determined by ANOVA with Tukey post-hoc (day 1 $n = 3$, days 3–21 $n = 4$); data represent mean \pm s.e.m. **i**, The loss in inflammation corresponds with an increase in vascularization, quantified by number of visible capillaries in histological sections; for *, $p < 0.05$ as determined by ANOVA with Tukey post-hoc ($n = 3$); data represent mean \pm s.e.m. **j**, An example tissue slice 10 days post injection shows an area of particularly high vascularization density (scale bar 100 μm). Additional images given in the Supplementary Information.

provides a stepwise means to tailor POP networks to specific applications. Towards this end, we envisage the following protocol to orthogonally tune POP properties: choose porosity with concentration; choose other physical properties (mechanical properties or T_i -cooling) with molecular weight, helix sequence and percentage; finally, choose aggregation temperature (T_i -heating) with ELP composition. The ability to tailor POP networks in this manner, and their ability to span two to three orders of magnitude in elastic moduli, could be useful, for example, in guiding stem cell differentiation, a mechanism fairly sensitive to the mechanical properties of the three-dimensional culture matrix that also requires control of matrix diffusivity to enable transport of nutrients and signalling factors to cells from the surrounding growth medium^{34,35}.

Our work departs in important ways from previous studies on block copolymers of bioactive or mechanically active folded protein domains with disordered sequences such as ELPs³⁶. Hydrogels and fibres have been produced with ordered segments such as coiled-coils and leucine-zippers to alter their self-assembly^{37,38}; however, these studies have focused on the specific impact of more complicated structural peptides rather than the modular incorporation of ordered versus disordered regions. Likewise, copolymers of disordered domains have produced gels and nanostructures^{39–41}, but these too lack the interplay of order and disorder as a design principle to encode higher-order structure. Recombinant combinations of peptide sequences derived from structural proteins such as collagen and silk with elastin are more closely related to

this study^{42,43}, although neither the precise and tunable control over thermal hysteresis nor the emergence of an interconnected thermally reversible fractal network architecture has been reported in these studies.

Combinations of order and disorder have also been explored in the field of synthetic polymers. Ratios of atactic (disordered) and isotactic (ordered) polymer blocks have long been used to control gelation, and even thermal phase transitions^{44,45}, with threshold percentages of isotactic polymers required for specific material properties. It is striking that the principles that guide the modification of synthetic polymers so readily align to those we have shown herein for bioinspired peptide polymers. Although synthetic polymers and recombinant peptide polymers each have their own advantages, peptide polymers are attractive for biotechnology and biomedical applications because of their native biocompatibility and our ability to design them at absolute molecular levels through recombinant synthesis, making them better suited for tuning material properties via precise—genetically encodable—changes of their amino acid sequence.

In situ network stability and cell penetration

POPs designed to transition below the body temperature (37°C) are advantageous for forming depots in vivo since they can be handled and injected as liquids, yet rapidly form viscoelastic materials when injected in vivo. Although injectable ELP depots have been used for controlled drug delivery⁴⁶, the homogenous liquid nature of non-crosslinked ELP coacervates has limited their applications in tissue engineering^{47,48}. Without chemical crosslinking, ELP coacervates lack the mechanical stability and porosity to support cell migration and growth⁴⁸. It has also been shown that porous materials interact more favourably with the immune system, preventing foreign body response and inducing the migration of regenerative immune cells^{49,50}. We posited that polypeptides such as POPs, which exhibit thermally triggered hierarchical self-assembly into stable porous networks without the need for chemical crosslinking, may have beneficial in vivo behaviours.

Motivated by this hypothesis, we next assessed the in vivo behaviour of injected POPs. We injected E1-H5-25%-120 (200 µl at 250 µM, 50 kDa) as sub-cutaneous depots and compared their pharmacokinetic (PK) properties to fully disordered ELPs of the same base sequence. POP depots, labelled with ¹²⁵I, showed substantially lower polymer release (4.8% of initial dose) than their disordered ELP counterparts (8.7%) after 120 h despite their increased porosity and greater surface area (Fig. 6a). Terminal bio-distribution also revealed no critical accumulation in vital organs (Supplementary Fig. 16). Upon injection, ELPs diffuse in the sub-cutaneous space until they are not visible externally, whereas POPs form large, visibly palpable depots (Fig. 6b). Single-photon emission computed tomography (SPECT) confirms that ELP depots are more diffuse than POP depots, with higher surface-to-volume ratios and lower polymer densities (Fig. 6c and Supplementary Fig. 17).

To analyse POP persistence in the sub-cutaneous space and cell recruitment, C57BL/6 mice receiving endotoxin purified (<1 endotoxin unit (EU) ml⁻¹) sub-cutaneous injections of E1-H5-25%-120 (200 µl at 250 µM, 50 kDa) were monitored over 21 days. Injected depots were excised and either fixed for histological evaluation or processed for flow cytometry (Supplementary Methods and Supplementary Figs. 18–20). POPs rapidly and robustly integrate into the sub-cutaneous space, creating mechanical connections with surrounding tissue within 24 h (Fig. 6e). Importantly, they do not show a significant decrease in size after 21 days (Fig. 6d and Supplementary Figs. 18,21). Initial cell recruitment is high, with cell density peaking at day 10 (Fig. 6f). Recruited cells show that the POP depots undergo a wound healing response with an initial, mild inflammatory phase that resolves over time, followed by angiogenesis and proliferation of non-immune cells. Haematopoietic-derived

cells (CD45+) steadily increase up to day 10, with neutrophils, inflammatory monocytes, and macrophages peaking on days 1, 3, and 10, respectively (Fig. 6g,h). By day 21, all haematopoietic derived cells drop off sharply and non-haematopoietic cells become the dominant population (Fig. 6g,h and Supplementary Fig. 21). Curiously, E1-H5-25%-120 injected at 750 µM POP showed minimal differences in recruited cell subtypes from the same POP injected at a concentration of 250 µM (Supplementary Fig. 21). As the explants from the 750 µM injections were larger, it is likely that the material was able to spread within the sub-cutaneous space, creating an effectively similar pore size in vivo. Histology of POP depots supports the presence of a high cellular density, extensive cellular infiltration from surrounding tissue, and a lack of fibrous capsule formation (Supplementary Fig. 22). POPs also show a high degree of vascularization, with capillaries and some larger vessels emerging by day 10—with some branching vessels visible even to the unaided eye (Fig. 6d,i,j). The vasculature becomes more uniformly distributed throughout the depots by day 21.

Because fully disordered ELPs diffuse too quickly to form explantable depots, we injected equivalent weight percentages of Matrigel for comparison. Given the biochemical differences between POPs and Matrigel, this comparison is intended only to provide a contrast to widely used temperature-sensitive, injectable scaffold. Compared to Matrigel, POPs recruit a greater number of cells, including non-haematopoietic cells, and show greatly increased mechanical integration and vascularization than Matrigel (Supplementary Fig. 23). POPs are probably more useful than Matrigel for applications requiring increased integration of the scaffold into surrounding tissue, whereas Matrigel may be more useful for applications requiring greater initial isolation of the material from surrounding tissue. The angiogenesis of POPs, with minimal inflammation, is promising for their use as injectable materials for regenerative medicine.

Summary and outlook

Using molecularly engineered polypeptides with precisely encoded ordered and disordered segments, we have developed a simple, modular and tunable material system to evaluate the impact of molecular order and disorder at the primary sequence level on the structure and properties of the resulting material. By encoding helical domains into ELPs, we show that thermally triggered phase separation does not lead to dense, homogeneous coacervates. Instead, POPs drive the hierarchical assembly of porous, physically cross-linked viscoelastic networks, architecturally reminiscent of cross-linked elastin. These networks retain the thermal reversibility of fully disordered ELPs; however, and rather strikingly, the aggregation and dissolution temperatures can be independently controlled by specifying the composition and mass fraction of the disordered and ordered domains. POPs assemble into 3D scaffolds in vivo that are notably more stable than fully disordered controls. Analysis of explanted POP depots reveals a progression from mild inflammation that resolves with time, to migration of cells within the scaffold, followed by proliferation and vascularization, indicating that POPs promote wound healing and tissue growth. As the field of intrinsically disordered proteins has expanded, knowledge of the biological importance of the synergy between disordered regions and ordered domains has grown; yet limited information exists on functionalizing these interactions for biomedical applications. Our biopolymer platform is an important step towards uncovering design rules that combine order and disorder to develop a new generation of functional protein-based biomaterials.

Online content

Any methods, additional references, Nature Research reporting summaries, source data, statements of data availability and associated accession codes are available at <https://doi.org/10.1038/s41567-018-0298-2>.

Received: 29 June 2017; Accepted: 29 August 2018;
Published online: 15 October 2018

References

- Keten, S., Xu, Z., Ihle, B. & Buehler, M. J. Nanoconfinement controls stiffness, strength and mechanical toughness of β -sheet crystals in silk. *Nat. Mater.* **9**, 359–367 (2010).
- Tamburro, A. M., Bochicchio, B. & Pepe, A. Dissection of human tropoelastin: exon-by-exon chemical synthesis and related conformational studies. *Biochemistry* **42**, 13347–13362 (2003).
- van der Lee, R. et al. Classification of intrinsically disordered regions and proteins. *Chem. Rev.* **114**, 6589–6631 (2014).
- Harmon, T. S., Holehouse, A. S., Rosen, M. K. & Pappu, R. V. Intrinsically disordered linkers determine the interplay between phase separation and gelation in multivalent proteins. *eLife* **6**, e30294 (2017).
- McDaniel, J. R., Mackay, J. A., Quiroz, F. G. & Chilkoti, A. Recursive directional ligation by plasmid reconstruction allows rapid and seamless cloning of oligomeric genes. *Biomacromolecules* **11**, 944–952 (2010).
- Roberts, S., Dzuricky, M. & Chilkoti, A. Elastin-like polypeptides as models of intrinsically disordered proteins. *FEBS Lett.* **589**, 2477–2486 (2015).
- McDaniel, J. R., Radford, D. C. & Chilkoti, A. A unified model for de novo design of elastin-like polypeptides with tunable inverse transition temperatures. *Biomacromolecules* **14**, 2866–2872 (2013).
- Pometun, M. S., Chekmenev, E. Y. & Wittebort, R. J. Quantitative observation of backbone disorder in native elastin. *J. Biol. Chem.* **279**, 7982–7987 (2004).
- MacEwan, S. R. & Chilkoti, A. Elastin-like polypeptides: biomedical applications of tunable biopolymers. *Biopolymers* **94**, 60–77 (2010).
- Gosline, J. et al. Elastic proteins: biological roles and mechanical properties. *Philos. Trans. R. Soc. B* **357**, 121–132 (2002).
- Lillie, M. A. & Gosline, J. M. The viscoelastic basis for the tensile strength of elastin. *Int. J. Biol. Macromol.* **30**, 119–127 (2002).
- Miller, J. S., Kennedy, R. J. & Kemp, D. S. Solubilized, spaced polyalanines: A context-free system for determining amino acid α -helix propensities. *J. Am. Chem. Soc.* **124**, 945–962 (2002).
- Chakrabarty, A. & Baldwin, R. Stability of α -Helices. *Adv. Protein Chem.* **46**, 141–176 (1995).
- Bochicchio, B., Pepe, A. & Tamburro, A. M. Investigating by CD the molecular mechanism of elasticity of elastomeric proteins. *Chirality* **20**, 985–994 (2008).
- Sreerama, N. & Woody, R. W. Estimation of protein secondary structure from circular dichroism spectra: Comparison of CONTIN, SELCON, and CDSSTR methods with an expanded reference set. *Anal. Biochem.* **287**, 252–260 (2000).
- Bernacki, J. P. & Murphy, R. M. Length-dependent aggregation of uninterrupted polyalanine peptides. *Biochemistry* **50**, 9200–9211 (2011).
- Muñoz, V. & Serrano, L. Elucidating the folding problem of helical peptides using empirical parameters. *Nat. Struct. Biol.* **1**, 399–409 (1994).
- Lacroix, E., Viguera, A. R. & Serrano, L. Elucidating the folding problem of α -helices: local motifs, long-range electrostatics, ionic-strength dependence and prediction of NMR parameters. *J. Mol. Biol.* **284**, 173–191 (1998).
- Wright, E. R., McMillan, R. A., Cooper, A., Apkarian, R. P. & Conticello, V. P. Thermoplastic elastomer hydrogels via self-assembly of an elastin-mimetic triblock polypeptide. *Adv. Funct. Mater.* **12**, 149–154 (2002).
- Glassman, M. J., Avery, R. K., Khademhosseini, A. & Olsen, B. D. Toughening of thermoresponsive arrested networks of elastin-like polypeptides to engineer cytocompatible tissue scaffolds. *Biomacromolecules* **17**, 415–426 (2016).
- Reguera, J. et al. Thermal behavior and kinetic analysis of the chain unfolding and refolding and of the concomitant nonpolar solvation and desolvation of two elastin-like polymers. *Macromolecules* **36**, 8470–8476 (2003).
- Cho, Y. et al. Hydrogen bonding of β -turn structure is stabilized in D_2O . *J. Am. Chem. Soc.* **131**, 15188–15193 (2009).
- Ding, F., Borreguero, J. M., Buldyrey, S. V., Stanley, H. E. & Dokholyan, N. V. Mechanism for the α -helix to β -hairpin transition. *Proteins* **53**, 220–228 (2003).
- Urry, D. W. & Ji, T. H. Distortions in circular dichroism patterns of particulate (or membranous) systems. *Arch. Biochem. Biophys.* **128**, 802–807 (1968).
- Urry, D. W., Starcher, B. & Partridge, S. M. Coacervation of solubilized elastin effects a notable conformational change. *Nature* **222**, 795–796 (1969).
- Muiznieks, L. D., Jensen, S. A. & Weiss, A. S. Structural changes and facilitated association of tropoelastin. *Arch. Biochem. Biophys.* **410**, 317–323 (2003).
- Yeo, G. C., Keeley, F. W. & Weiss, A. S. Coacervation of tropoelastin. *Adv. Colloid. Interface Sci.* **167**, 94–103 (2011).
- Israelachvili, J. N., Mitchell, D. J. & Ninham, B. W. Theory of self-assembly of hydrocarbon amphiphiles into micelles and bilayers. *J. Chem. Soc. Faraday Trans. 1* **72**, 1525–1568 (1976).
- Dušek, K. Phase separation during the formation of three-dimensional polymers. *J. Polym. Sci. B* **3**, 209–212 (1965).
- Cirulis, J. T., Keeley, F. W. & James, D. F. Viscoelastic properties and gelation of an elastin-like polypeptide. *J. Rheol.* **53**, 1215 (2009).
- Tamburro, A. M., De Stradis, A. & D'Alessio, L. Fractal aspects of elastin supramolecular organization. *J. Biomol. Struct. Dyn.* **12**, 1161–1172 (1995).
- Gustafsson, M. G. Nonlinear structured-illumination microscopy: wide-field fluorescence imaging with theoretically unlimited resolution. *Proc. Natl Acad. Sci. USA* **102**, 13081–13086 (2005).
- Clarke, A. W. et al. Tropoelastin massively associates during coacervation to form quantized protein spheres. *Biochemistry* **45**, 9989–9996 (2006).
- Caiazza, M. et al. Defined three-dimensional microenvironments boost induction of pluripotency. *Nat. Mater.* **15**, 344–352 (2016).
- Engler, A. J., Sen, S., Sweeney, H. L. & Discher, D. E. Matrix elasticity directs stem cell lineage specification. *Cell* **126**, 677–689 (2006).
- DiMarco, R. L. & Heilshorn, S. C. Multifunctional materials through modular protein engineering. *Adv. Mater.* **24**, 3923–3940 (2012).
- Fernandez-Colino, A., Arias, F. J., Alonso, M. & Rodriguez-Cabello, J. C. Amphiphilic elastin-like block co-recombinamers containing leucine zippers: Cooperative interplay between both domains results in injectable and stable hydrogels. *Biomacromolecules* **16**, 3389–3398 (2015).
- Xu, C. & Kopecek, J. Genetically engineered block copolymers: influence of the length and structure of the coiled-coil blocks on hydrogel self-assembly. *Pharm. Res.* **25**, 674–682 (2008).
- Wright, E. R. & Conticello, V. P. Self-assembly of block copolymers derived from elastin-mimetic polypeptide sequences. *Adv. Drug Deliv. Rev.* **54**, 1057–1073 (2002).
- Martin, L., Castro, E., Ribeiro, A., Alonso, M. & Rodriguez-Cabello, J. C. Temperature-triggered self-assembly of elastin-like block co-recombinamers: the controlled formation of micelles and vesicles in an aqueous medium. *Biomacromolecules* **13**, 293–298 (2012).
- MacEwan, S. R. et al. Phase behavior and self-assembly of perfectly sequence-defined and monodisperse multiblock copolypeptides. *Biomacromolecules* **18**, 599–609 (2017).
- Xia, X. X., Xu, Q., Hu, X., Qin, G. & Kaplan, D. L. Tunable self-assembly of genetically engineered silk–elastin-like protein polymers. *Biomacromolecules* **12**, 3844–3850 (2011).
- Luo, T. & Kiick, K. L. Noncovalent modulation of the inverse temperature transition and self-assembly of elastin-b-collagen-like peptide bioconjugates. *J. Am. Chem. Soc.* **137**, 15362–15365 (2015).
- Ray, B., El Hasri, S. & Guenet, J. M. Effect of polymer tacticity on the molecular structure of polyelectrolyte/surfactant stoichiometric complexes in solutions and gels. *Eur. Phys. J. E* **11**, 315–323 (2003).
- Ray, B. et al. Effect of tacticity of poly(N-isopropylacrylamide) on the phase separation temperature of its aqueous solutions. *Polym. J.* **37**, 234–237 (2005).
- Amiram, M., Luginbuhl, K. M., Li, X., Feinglos, M. N. & Chilkoti, A. Injectable protease-operated depots of glucagon-like peptide-1 provide extended and tunable glucose control. *Proc. Natl Acad. Sci. USA* **110**, 2792–2797 (2013).
- Nettles, D. L., Chilkoti, A. & Setton, L. A. Applications of elastin-like polypeptides in tissue engineering. *Adv. Drug Deliv. Rev.* **62**, 1479–1485 (2010).
- Nettles, D. L. et al. In situ crosslinking elastin-like polypeptide gels for application to articular cartilage repair in a goat osteochondral defect model. *Tissue Eng. Part A* **14**, 1133–1140 (2008).
- Ratner, B. D. A pore way to heal and regenerate: 21st century thinking on biocompatibility. *Regen. Biomater.* **3**, 107–110 (2016).
- Sussman, E. M., Halpin, M. C., Muster, J., Moon, R. T. & Ratner, B. D. Porous implants modulate healing and induce shifts in local macrophage polarization in the foreign body reaction. *Ann. Biomed. Eng.* **42**, 1508–1516 (2014).

Acknowledgements

We thank K. Wang for his invaluable help with SIM imaging and E. Betzig for use of his facilities at Janelia Farms for SIM. This work was funded by the NIH through grants GM061232 to A.C. and R01NS056114 to R.V.P., by the NSF through grants from the Research Triangle MRSEC (DMR-11-21107), NSF DMFREF (DMR-1729671) to A.C., MCB-1614766 to R.V.P., and through the Graduate Research Fellowship Program under grant no. 1106401 to S.R.

Author Contributions

S.R. designed and performed experiments, analysed data and prepared the manuscript. T.S.H. designed and performed the coarse-grained simulations and co-developed the phenomenological model for hysteresis. J.L.S. designed, performed and analysed in vivo work. K.L. designed and performed structural characterization with NMR and CD. A.H. and V.M. constructed POPs and characterized their phase behaviour. V.M. also performed rheological experiments. Y.W. designed and aided in vivo experiments. T.O.

provided guidance and analysed data for POP structural characterization. J.C. provided guidance for in vivo experiments. R.V.P. provided guidance, developed the conceptual framework for hysteresis, analysed results from the coarse-grained simulations, and contributed to preparing the manuscript. A.C. provided guidance, designed experiments and prepared the manuscript. All authors participated in discussion of the data and in editing and revising the manuscript.

Competing Interests

The authors declare no competing interests for this work.

Additional information

Supplementary information is available for this paper at <https://doi.org/10.1038/s41563-018-0182-6>.

Reprints and permissions information is available at www.nature.com/reprints.

Correspondence and requests for materials should be addressed to A.C.

Publisher's note: Springer Nature remains neutral with regard to jurisdictional claims in published maps and institutional affiliations.

© The Author(s), under exclusive licence to Springer Nature Limited 2018

Methods

Synthesis of polymer genes. All polymers were cloned into a modified pet24 vector using a previously described process known as recursive directional ligation by plasmid reconstruction (PRE-RDL)². Briefly, single-stranded oligomers encoding the desired sequences were annealed into cassettes with CC and GG overhangs. The overhangs enabled their concatemerization and ligation (Quick Ligase, NEB) into the pet24 vector. Using this process, we created a library of elastin-like polypeptide and polyalanine cassettes (Supplemental Table 1), which could be strung together through multiple cycles of PRE-RDL to form the final partially ordered polymers. All of the base oligomer cassettes used for polymer construction can be found below. Plasmids were transfected into chemically competent Eb5α (EdgeBio) cells for cloning and BL21(DE3) (EdgeBio) cells for protein expression.

Expression and purification of POPs. For protein expression, 5 ml starter cultures were grown overnight from -80°C dimethylsulfoxide stocks. Cells were then pelleted, resuspended in 1 ml of terrific broth, and used, along with 1 ml $100\text{ }\mu\text{g ml}^{-1}$ of kanamycin (EMD Millipore) to inoculate 1 l of media. Cells were shaken at 200 r.p.m. for 8 h at 25°C before induction. For induction of protein expression, 1 ml of 1 M isopropyl β -D-1-thiogalactopyranoside (Goldbio) was added to the flask and cultures were placed at 16°C and 200 r.p.m. overnight. Expression at lower temperature was necessary to prevent the formation of truncation products at ELP–polyalanine junctions. Cells were then pelleted and resuspended in 10 ml of 1X phosphate buffered saline (PBS) for every 1 l of culture grown. Pulse sonication on ice, with a total active time of 3 min, was used to lyse cells. Cell lysates were treated with 10% polyethylenimine (PEI) (MP Biomedical) (2 ml l^{-1} culture) to remove contaminating DNA and centrifuged at 14,000 r.p.m. for 10 min at 4°C . Polymer was purified from the resulting soluble fraction using a modified version of inverse thermal cycling³¹. The fraction was heated to 65°C or until phase separation was observed. For more hydrophilic polymers, this often required the addition of 1–2 M NaCl to depress the transition temperature. Once aggregated, the polymer solutions were centrifuged at 14,000 r.p.m. for 10 min at 35°C (note that a specific r.p.m./r.c.f. is not required as long as clear separation can be seen between the aggregated and soluble phases), and the resulting pellet was re-suspended in 5–10 ml PBS. The heating and cooling centrifugation cycles were repeated two to three more times until a purity of 95% was achieved, as analysed by sodium dodecyl sulfate polyacrylamide gel electrophoresis (SDS-PAGE). Purified polymers were dialysed at 4°C with frequent water changes for two days and lyophilized for storage. Final purity and homogeneity were verified by SDS-PAGE, and their molecular weights were verified by matrix-assisted laser desorption ionization mass spectrometry (MALDI-MS); in all cases, the experimentally determined molecular weights agreed with their theoretical molecular weights within 2%.

Secondary structure characterization. Circular dichroism experiments were performed using an Aviv Model 202 instrument and 1 mm quartz cells (Hellma USA). Unless otherwise noted, scans were carried out in PBS (pH = 7.4) with a polymer concentration of $10\text{ }\mu\text{M}$. Polymers were scanned in triplicate from 260 nm to 185 nm in 1 nm steps with a 1 s averaging time. Data points with a dynode voltage above 500 V were ignored in the analysis. All measurements were performed at 20°C unless otherwise specified. Temperature ramping was done in $5^{\circ}\text{C min}^{-1}$ increments with a 1 min equilibration at each step. A detailed description of NMR experiments is given in the Supplementary Information. In brief, polymers were grown in M9 minimal media with $^{15}\text{N-NH}_4\text{Cl}$ and ^{13}C -Glucose (Cambridge Isotopes) to label the nitrogen and carbons for triple-resonance measurements. Helicity was determined based on the alanine peaks of the H(N)CO spectra for E1–H2–25% after resonance assignment.

Temperature-dependent turbidity. The transition temperature (T_i) of each sample was determined by monitoring the optical density at 350 nm as a function of temperature on a UV–Vis spectrophotometer (Cary 300 Bio; Varian Instruments) equipped with a multicell thermoelectric temperature controller. The value of T_i was defined as the point of largest inflection (maximum of the first derivative) for the optical density. Unless otherwise stated, all samples were heated and cooled at $1^{\circ}\text{C min}^{-1}$ in PBS at concentrations between 10 and $1,000\text{ }\mu\text{M}$.

Coarse-grained molecular dynamics simulations. See Supplementary Information.

Rheology. Before performing oscillatory shear rheology, samples were prepared in PBS and allowed to equilibrate at 4°C . Measurements were taken on a Kinexus Pro (Malvern) using a Peltier heating element and a 10 mm parallel plate geometry. Samples were enclosed in a humidified environment to prevent drying during heating, equilibration and oscillation. Soluble polymer samples were loaded onto the lower portion of the geometry set at 4°C . The upper portion of the geometry was lowered to 0.5 mm, and the instrument was subsequently heated to the experimental temperature (37°C unless otherwise specified) and allowed to equilibrate for 30 min. To account for volume contraction in ELP and POP gels, samples were run with a normal force control of 0.1 N—determined to be the optimal normal force to maintain geometry contact without sample deformation.

Uncrosslinked ELP gels were too soft for adequate normal force control, and were instead run with a gap control set to the average gap of their corresponding POP concentration. Each polymer condition was repeated in triplicate. For comparison to chemical crosslinking, an additional ELP (E1₃₀DK) was produced which matched the aspartic acid and lysine distribution of E1–H5–25%, with otherwise identical composition to E1₃₀. Tetrakis(hydroxymethyl)phosphonium chloride (THPC) was used to crosslink available lysines, and, unless otherwise stated, crosslinker was mixed in a 1:1 molar ratio with polymer lysines (a 4:1 molar ratio with polymer). THPC was added to the polymer solution at 4°C before heating and equilibration.

Fluorescence imaging and analysis. POPs were fluorescently labelled using Alexa Fluor 488 NHS Ester (Thermo Fisher) with a typical reaction efficiency of 20%. Excess dye was removed with dialysis and polymers were lyophilized for storage. For all experiments, the dyed polymers were diluted into an undyed stock such that no more than 5% of POPs in solution were labelled. Confocal images were taken on a Zeiss 710 inverted microscope with temperature-controlled incubation. To prevent dehydration, 50 μl of sample solution was added to 384-well #1.5 glass bottom plates (Cellvis) for imaging. Solutions were added below the T_i , allowed to transition and equilibrated for 5 min on the microscope stage. For FRAP experiments, samples ($n = 3$ for each group) were equilibrated for 30 min to prevent thermal movement of the focusing stage, and fluorescence intensity analysis was done using Zen software (ZEISS Microscopy). Samples were bleached for 30 s at 90% laser power, and images were collected every 5 s for 30 min. Unbleached areas were taken at the same time and fluorescence values were normalized to changes in unbleached areas to account for natural photobleaching with continued laser exposure. For void volume analysis, 20 μm image stacks ($n = 3$ for each concentration) were taken with a pinhole size of 1 Airy unit and vertical slice intervals of 230 nm. Three-dimensional reconstructions of the resultant networks and quantification of their void volume were done in IMARIS 8 (Bitplane). Surface renders were constructed with a minimum object detail of 200 nm, the minimal lateral resolution of the confocal microscope, and local background thresholding with the diameter of the largest sphere that fits into the object set at $1\text{ }\mu\text{m}$. A consistent minimum background threshold was used across samples. Network fractal dimensions were determined using the two-dimensional box counting algorithm from the FracLac plugin for ImageJ^{32,33}. Structured illumination microscopy images were taken with assistance from K. Wang using an in-house microscope constructed at Janelia Farm in the lab of E. Betzig. Polymer samples were added to a glass slide at 4°C and allowed to aggregate and equilibrate at 37°C . After equilibration, a cover slip was added, since the SIM was an upright microscope, resulting in some network deformation on the microscale as compared to the confocal images. SIM images were taken with a lateral resolution of $\sim 120\text{ nm}$ and an axial resolution of $\sim 300\text{ nm}$. Image stacks were acquired with a z-distance of 150 nm, and 15 SIM images were taken for each plane—five phases and three angles. Voxel size for all reconstructed images—done using an in-house algorithm—was 48 nm in x,y and 147 nm in z. Reconstructed image stacks of $5\text{ }\mu\text{m}$ were used to create maximum intensity projections for analysis in ImageJ. Additional technical details on the experimental set-up have been previously published^{34,35}.

Pharmacokinetic and SPECT analysis. All constructs were endotoxin-purified to $< 1\text{ EU ml}^{-1}$, prepared at $500\text{ }\mu\text{M}$ in sterilized PBS and reacted with ^{125}I (Perkin Elmer) in Pierce pre-coated IODOGEN tubes (Fisher Scientific)³⁶. The product was centrifugally purified through 40 K MWCO Zeba Spin Desalting Columns (Thermo Scientific) at 2,500 r.p.m. for 3 min at 4°C to remove unreacted radioiodine from the conjugate. After labelling, each construct was diluted down to a final biopolymer concentration of $250\text{ }\mu\text{M}$. The resulting activity dose for the POP was 1.18 mCi ml^{-1} , while the ELP dose was 1.37 mCi ml^{-1} .

Female athymic nude mice (7 weeks old) were purchased from Charles River and housed in a centralized animal facility at Duke University. All procedures were approved by the Duke University Institutional Animal Care and Use Committee and were in compliance with the NIH Guide for the Care and Use of Laboratory Animals. 50 μl of the POP was prepared in an Eppendorf tube at $63\text{ }\mu\text{Ci}$ to provide a reference imaging standard. Before either the depot injection, blood draw, or single-photon emission computed tomography (SPECT) imaging, each mouse was anaesthetized using a 1.6% isoflurane vaporizer feed at an O_2 flow rate of 0.61 min^{-1} . For depot injections, each mouse received a soluble 200 μl injection of their respective solution at $250\text{ }\mu\text{M}$ into the subcutaneous space on the right hind flank. The whole body activity of the mouse was then measured in an AtomLab 400 dose calibrator (Biodex). A total of 12 athymic nude mice ($n = 6$ for each group) were used for pharmacokinetic analysis of depot stability and distribution. An initial 10 μl blood sample was drawn and pipetted into $1,000\text{ mg ml}^{-1}$ heparin with subsequent blood draws at time points of 45 min and 4, 8, 24, 48, 72, 96 and 120 h to determine the release profile for the depots. A total of six athymic nude mice also were imaged using SPECT at time points of 0, 48 and 120 h. Mice were then transferred under anaesthesia to the bed of the U-SPECT-II/CT for imaging using a 0.350 collimator (MILabs B.V.) courtesy of G. A. Johnson in the Duke CIVM. Anaesthesia was maintained with a 1.6% isoflurane feed at an O_2 flow rate of 0.61 min^{-1} . SPECT acquisition was conducted over a time frame of 15 min in

'list-mode' and at a 'fine' step-mode. Upon completion, a subsequent CT scan was carried out at a current of 615 μ A and a voltage of 65 kV. Mice were then returned to their cages. Post-imaging SPECT reconstruction was carried out using MILabs proprietary software without decay correction and centred on the 125 I photon range of 15–45 keV. All images were reconstructed at a voxel size of 0.2 mm. Reconstructed SPECT images were then registered with their corresponding CT scans to provide spatial alignment for anatomical reference.

On completion of the study, all mice were euthanized and dissected. The subcutaneous depots were excised and visually examined for physical differences. In addition, the heart, thyroid, lungs, liver, kidneys, spleen, skin, muscle and pancreas were collected and analysed using a Wallac 1282 Gamma Counter (Perkin Elmer) to determine the relative biodistribution of the different constructs. All blood samples and the set of PK standards were similarly analysed using the gamma counter. The counts per minute detected for each sample were converted to their corresponding activity. Blood samples were then scaled to determine the total amount in circulation according to the formula³⁷ $\text{Total} = \text{CPM}/.01 \times \text{BW} \times 72 \text{ ml kg}^{-1}$, where CPM is counts per minute and BW is body weight. Depot retention was analysed by measuring the total photon intensity of the depot SPECT image in ImageJ. Measured photon intensity was converted to total depot activity using a calibration factor determined from the imaging standard. This calibration was determined by performing a linear regression of the known activities of the standard over time against the corresponding SPECT intensity measurements. The factor was applied to each depot and the calculated activity compared against the original whole body injected dose at 0 h to determine its percentage retention.

Cell recruitment. Female C57BL/6 mice (7 weeks old) were purchased from Charles River and housed in a centralized animal facility at Duke University. All procedures were approved by the Duke University Institutional Animal Care and Use Committee and were in compliance with the NIH Guide for the Care and Use of Laboratory Animals. For analysis of POP persistence and cell recruitment, female C57BL/6 mice (used for their complete immune system over the nude mice used in the previous study for easier depot observation) received soluble injections in the subcutaneous space of the right and left hind flanks. Mice were injected with either 200 μ l of 250 μ M E1-H5-25%-120 ($n=19$), 200 μ l of 750 μ M E1-H5-25%-120 ($n=4$), or Matrigel (Standard Formulation, Corning) ($n=7$). POPs were endotoxin-purified to $<1 \text{ EU ml}^{-1}$ and sterile filtered before injection. At respective time points, mice were euthanized and dissected. Left hind injections were excised and placed in 10% neutral buffered formalin (Sigma) for histological analysis ($n=3$ for all groups). Fixed depots were embedded in paraffin, and 5 μ m slices from the centre of each depot were stained with Haematoxylin and Eosin (H&E). H&E-stained slides were imaged using an Axio 506 colour camera mounted on a Zeiss Axio Imager Widefield microscope. Images at 200 \times magnification were stitched and exported for analysis. Blood vessels and capillaries were manually counted in ImageJ ($n=3$). For changes in depot size, images of excised depots were taken at a controlled distance and imported into ImageJ for quantification.

Flow cytometry experimental details, including staining, acquisition and gating, are given in the Supplementary Information. In brief, excised injections were digested, filtered to attain a single-cell suspension and stained with markers for haematopoietic cell subtypes (neutrophils, monocytes, macrophages) and non-haematopoietic subtypes (epithelial and endothelial).

Statistics and reproducibility. All statistical analysis was carried out using Prism 6 (Graphpad Inc.). Where box and whisker plots are used, the centreline represents the median, the box limits represent the upper and lower quartiles, and the whiskers represent a range of 10–90% of the maximum. Where bar charts are used, individual data points are provided along with standard error (s.e.m.) error bars unless otherwise specified. When comparing individual groups, two-tailed t-tests were used to determine statistical significance. Analysis of variance (ANOVA) was used to evaluate significance among three or more groups and the Tukey–Kramer or Dunnett's methods were used as post hoc tests where indicated in the text for comparisons between groups. Experimental group sizes are given within the descriptions of each experiment.

All CD, optical density, microscopy (confocal and SIM), rheology, and light scattering experiments were repeated at least three times, with similar results. NMR spectral analysis was repeated twice, with similar results. Polymers were purified several times from independent stocks to ensure observed behaviour was not batch dependent. For animal experiments, repetition was conducted where possible without unnecessary use of animals. Histological evaluations were repeated at least three times, with similar results, and where representative images are used in the main text (for example, SPECT and explanted depots) a range of additional images are provided in the Supplementary Information.

Reporting Summary. Further information on research design is available in the Nature Research Reporting Summary linked to this article.

Data availability

The authors declare that all data supporting the findings of this study are available within the manuscript and its supplementary files and are available from the authors on reasonable request.

References

- Meyer, D. E. & Chilkoti, A. Purification of recombinant proteins by fusion with thermally-responsive polypeptides. *Nat. Biotechnol.* **17**, 1112–1115 (1999).
- Schneider, C. A., Rasband, W. S. & Eliceiri, K. W. NIH Image to ImageJ: 25 years of image analysis. *Nat. Methods* **9**, 671–675 (2012).
- Karperien, A. FracLac for ImageJ, version 2.5 <http://rsb.info.nih.gov/ij/plugins/fracLac/FLHelp/Introduction.html> (1999–2013).
- Shao, L., Kner, P., Rego, E. H. & Gustafsson, M. G. Super-resolution 3D microscopy of live whole cells using structured illumination. *Nat. Methods* **8**, 1044–1046 (2011).
- Gustafsson, M. G. et al. Three-dimensional resolution doubling in wide-field fluorescence microscopy by structured illumination. *Biophys. J.* **94**, 4957–4970 (2008).
- Wood, W. G., Wachter, C. & Scriba, P. C. Experiences using chloramine-T and 1,3,4,6-tetrachloro-3- α ,6- α -Diphenylglycoluril (Iodogen[®]) for radioiodination of materials for radioimmunoassay. *J. Clin. Chem. Clin. Bio.* **19**, 1051–1056 (1981).
- Diehl, K. H. et al. A good practice guide to the administration of substances and removal of blood, including routes and volumes. *J. Appl. Toxicol.* **21**, 15–23 (2001).

Reporting Summary

Nature Research wishes to improve the reproducibility of the work that we publish. This form provides structure for consistency and transparency in reporting. For further information on Nature Research policies, see [Authors & Referees](#) and the [Editorial Policy Checklist](#).

Statistical parameters

When statistical analyses are reported, confirm that the following items are present in the relevant location (e.g. figure legend, table legend, main text, or Methods section).

n/a Confirmed

- ☐ ☒ The exact sample size (n) for each experimental group/condition, given as a discrete number and unit of measurement
- ☐ ☒ An indication of whether measurements were taken from distinct samples or whether the same sample was measured repeatedly
- ☐ ☒ The statistical test(s) used AND whether they are one- or two-sided
Only common tests should be described solely by name; describe more complex techniques in the Methods section.
- ☐ ☒ A description of all covariates tested
- ☐ ☒ A description of any assumptions or corrections, such as tests of normality and adjustment for multiple comparisons
- ☐ ☒ A full description of the statistics including central tendency (e.g. means) or other basic estimates (e.g. regression coefficient) AND variation (e.g. standard deviation) or associated estimates of uncertainty (e.g. confidence intervals)
- ☐ ☒ For null hypothesis testing, the test statistic (e.g. F , t , r) with confidence intervals, effect sizes, degrees of freedom and P value noted
Give P values as exact values whenever suitable.
- ☐ ☒ For Bayesian analysis, information on the choice of priors and Markov chain Monte Carlo settings
- ☐ ☒ For hierarchical and complex designs, identification of the appropriate level for tests and full reporting of outcomes
- ☐ ☒ Estimates of effect sizes (e.g. Cohen's d , Pearson's r), indicating how they were calculated
- ☐ ☒ Clearly defined error bars
State explicitly what error bars represent (e.g. SD, SE, CI)

Our web collection on [statistics for biologists](#) may be useful.

Software and code

Policy information about [availability of computer code](#)

Data collection

No custom code was used to collect data. All data were collected using the commercial programs provided with the instruments used as discussed in the manuscript methods.

Data analysis

No custom code was used to analyze data. Analysis was primarily done in Microsoft Excel and Prism. ImagJ, Flowjo, NMRviewJ, and IMARIS were also used as detailed in the manuscript methods.

For manuscripts utilizing custom algorithms or software that are central to the research but not yet described in published literature, software must be made available to editors/reviewers upon request. We strongly encourage code deposition in a community repository (e.g. GitHub). See the Nature Research [guidelines for submitting code & software](#) for further information.

Data

Policy information about [availability of data](#)

All manuscripts must include a [data availability statement](#). This statement should provide the following information, where applicable:

- Accession codes, unique identifiers, or web links for publicly available datasets
- A list of figures that have associated raw data
- A description of any restrictions on data availability

The authors declare that all data supporting the findings of this study are available within the manuscript and its supplementary files and are available from the authors on reasonable request.

Field-specific reporting

Please select the best fit for your research. If you are not sure, read the appropriate sections before making your selection.

☒ Life sciences ☐ Behavioural & social sciences ☐ Ecological, evolutionary & environmental sciences

For a reference copy of the document with all sections, see [nature.com/authors/policies/ReportingSummary-flat.pdf](https://www.nature.com/authors/policies/ReportingSummary-flat.pdf)

Life sciences study design

All studies must disclose on these points even when the disclosure is negative.

Sample size	Sample sizes were determined based on the number of samples required for statistical comparisons between groups.
Data exclusions	None.
Replication	All attempts at replication were successful.
Randomization	No randomization was required for non-animal work. For animal experiments, mice were randomized prior to handling, and all mice were treated with identical measures prior to selection.
Blinding	Blinding was not relevant to this work as no experimental treatments requiring this method were used.

Reporting for specific materials, systems and methods

Materials & experimental systems

n/a	Involved in the study
<input checked="" type="checkbox"/>	<input type="checkbox"/> Unique biological materials
<input type="checkbox"/>	<input checked="" type="checkbox"/> Antibodies
<input checked="" type="checkbox"/>	<input type="checkbox"/> Eukaryotic cell lines
<input checked="" type="checkbox"/>	<input type="checkbox"/> Palaeontology
<input type="checkbox"/>	<input checked="" type="checkbox"/> Animals and other organisms
<input checked="" type="checkbox"/>	<input type="checkbox"/> Human research participants

Methods

n/a	Involved in the study
<input checked="" type="checkbox"/>	<input type="checkbox"/> ChIP-seq
<input type="checkbox"/>	<input checked="" type="checkbox"/> Flow cytometry
<input checked="" type="checkbox"/>	<input type="checkbox"/> MRI-based neuroimaging

Antibodies

Antibodies used	Anti-mouse CD45-BV-510 (30-F11, BD Biosciences, San Jose, CA), F4/80-PerCP-Cy5.5 (BM8, Biolegend, San Diego, CA), CD11b-APC (M1/70, Biolegend, San Diego, CA), Ly6C-FITC (AL-21 Biolegend, San Diego, CA), Ly6G-PE (IA8, Biolegend, San Diego, CA), CD31-PE-Cy7 (390, Biolegend, San Diego, CA), CD326-APC-Cy7 (G8.8, Biolegend, San Diego, CA), and DAPI (Biolegend, San Diego, CA) were used for flow cytometry analysis.
Validation	Validation statements were provided by the manufacturer, and fluorescence intensities were further validated by absorption onto AbC control beads (Thermo Fisher, Waltham, MA).

Animals and other organisms

Policy information about [studies involving animals](#); [ARRIVE guidelines](#) recommended for reporting animal research

Laboratory animals	For PK and SPECT analysis, 7 week old female athymic nude mice were purchased from Charles River. For cell infiltration analysis, 7 week old female C57BL/6 mice were purchased from Charles River.
Wild animals	None.
Field-collected samples	None.

Flow Cytometry

Plots

Confirm that:

- ☒ The axis labels state the marker and fluorochrome used (e.g. CD4-FITC).
- ☒ The axis scales are clearly visible. Include numbers along axes only for bottom left plot of group (a 'group' is an analysis of identical markers).
- ☒ All plots are contour plots with outliers or pseudocolor plots.
- ☒ A numerical value for number of cells or percentage (with statistics) is provided.

Methodology

Sample preparation	Excised right hind injections (n=3-4) were transferred to 2ml PBS and digested with 0.5mg/ml Collagenase IV (Sigma, St. Louis, MO) and 50 units of DNase I (Sigma, St. Louis, MO) at 37°C for 45min. Digested tissue was filtered through a 70um cell strainer and repeatedly washed with sterile 2% FBS (Thermo Fisher, Waltham, MA) in PBS. After ACK (Thermo Fisher, Waltham, MA) lysis, cells were counted using a hemocytometer. Cells were stained as previously described by others. Briefly, cells were blocked with 2.4 G2 antibody (BD Biosciences, San Jose, CA) and stained antibody mixture.
Instrument	Cell type analysis was done on a FACSCANTO II (BD Biosciences, San Jose, CA).
Software	Flow cytometry data was gated and quantified with FlowJo (FlowJo LLC, Portland, Oregon) and exported for analysis.
Cell population abundance	Flow cytometry was used for analysis purposes only, not to isolated cell populations for further use. Relative abundance of specific cell types changes between experimental groups and is discussed withing the main text and supplemental information of the manuscript.
Gating strategy	Cell debris was removed using SSC-A vs FSC-A, singlets were isolated using FSC-A vs FSC-H, and live cells were isolated using DAPI vs FSC-A. >50k live cells were quantified for each experiement before cell analysis was stopped.

- ☒ Tick this box to confirm that a figure exemplifying the gating strategy is provided in the Supplementary Information.